



**HAL**  
open science

## Poloidal localization of the explosive onset of edge localized modes

E. Trier, P. Hennequin, M. Maraschek, L. Giannone, B. Vanovac

► **To cite this version:**

E. Trier, P. Hennequin, M. Maraschek, L. Giannone, B. Vanovac. Poloidal localization of the explosive onset of edge localized modes. *Nuclear Fusion*, 2024, 64 (2), pp.026004. 10.1088/1741-4326/ad13ae . hal-04415010

**HAL Id: hal-04415010**

**<https://hal.science/hal-04415010>**

Submitted on 24 Jan 2024

**HAL** is a multi-disciplinary open access archive for the deposit and dissemination of scientific research documents, whether they are published or not. The documents may come from teaching and research institutions in France or abroad, or from public or private research centers.

L'archive ouverte pluridisciplinaire **HAL**, est destinée au dépôt et à la diffusion de documents scientifiques de niveau recherche, publiés ou non, émanant des établissements d'enseignement et de recherche français ou étrangers, des laboratoires publics ou privés.

# Poloidal localization of the explosive onset of edge localized modes

E. Trier<sup>1,a,\*</sup>, P. Hennequin<sup>2</sup>, M. Maraschek<sup>1</sup>, L. Giannone<sup>1</sup>, B. Vanovac<sup>1,b</sup> and the ASDEX Upgrade Team<sup>1,c</sup>

<sup>1</sup> Max Planck Institute for Plasma Physics, D-85748 Garching, Germany

<sup>2</sup> Laboratoire de Physique des Plasmas, Ecole Polytechnique, CNRS, F-91128 Palaiseau Cedex, France

E-mail: [elisee.trier@polytechnique.edu](mailto:elisee.trier@polytechnique.edu)

Received 13 September 2023, revised 17 November 2023

Accepted for publication 8 December 2023

Published 19 December 2023



CrossMark

## Abstract

In ASDEX Upgrade lower single null H-mode plasmas, the onset of the explosive phase of Edge Localized Modes (ELMs) is poloidally localized in the X-point/outer strike point (X/OSP) region. From this location, ELMs develop on average towards the low-field and high-field sides in typically 100  $\mu$ s. An associated magnetic activity localized in the X/OSP region is also observed in-between ELMs, at a lower level than at the ELM onset, and interpreted as being due to perturbed currents connected to the divertor target-s. Its broadband spectra typically extend up to 100 kHz—due to short-lived events of variable frequencies—and are dominated by  $n = 1$  toroidal mode numbers rotating in the counter-current direction.

Keywords: tokamaks, magnetic fluctuations, ELMs

## 1. Introduction

In tokamaks, the plasma confinement is improved when an edge transport barrier forms, creating a local region of reduced turbulent transport and steep pressure gradient. The corresponding regime, named H-mode, will be part of the baseline scenario for ITER. The edge transport barrier is frequently subject to Edge Localized Modes (ELMs), which are events causing an abrupt loss of particles and energy. Their mitigation is an active area of research, as the predicted ELM-induced power fluxes could exceed the maximum value tolerated by the divertor targets in future machines [1].

<sup>a</sup> Current affiliation: UKAEA, Culham Science Centre, Abingdon OX14 3DB, United Kingdom.

<sup>b</sup> Current affiliation: Massachusetts Institute of Technology, Plasma Science and Fusion Center, Cambridge, MA 02139, United States of America.

<sup>c</sup> See Stroth *et al* 2022 (<https://doi.org/10.1088/1741-4326/ac207f>) for the ASDEX Upgrade Team.

\* Author to whom any correspondence should be addressed.



Original Content from this work may be used under the terms of the [Creative Commons Attribution 4.0 licence](https://creativecommons.org/licenses/by/4.0/). Any further distribution of this work must maintain attribution to the author(s) and the title of the work, journal citation and DOI.

The mechanism causing the ELM crash is not fully understood. The peeling–ballooning theory [2] has been successful at predicting the value of edge parameters such as the pressure gradient and the current density at the onset of ELMs. However, the plasma edge can remain during a long period (several ms, while a crash typically develops in 100  $\mu$ s) close to the corresponding linear instability boundary before an ELM is triggered. Moreover, a recent study at JET [3] observed long-lived peeling–ballooning modes at a saturated level tens of milliseconds before an ELM crash. This leads to the suspicion that additional physics may be required to fully describe an ELM. Experimentally, several types of inter-ELM fluctuations are observed (see the recent review [4] and references therein), and some modes were shown to be related to the ELM onset [5–10]. However, no ELM trigger has been robustly identified so far.

The main result of this article is the observation that the start of the explosive phase of ELMs is poloidally localized in the X-point/outer strike point (X/OSP) region. The term ‘explosive’ here refers to a growth phase of typical duration 20–50  $\mu$ s, which is short in comparison with the typical lifetime of inter-ELM modes (several ms) or changes of magnetic activity occurring before an ELM ( $\sim$ 1 ms).

The magnetic perturbations in the X/OSP region are also present during the inter-ELM phases, at a lower level. Its inter-ELM properties will be described and shown to differ significantly from those of the magnetic activity coming from the confined region.

The paper is organized as follows: in section 2, the diagnostics and the studied plasmas are described. Section 3 presents the observation of a poloidally localized start of the ELMs explosive phase. The inter-ELM properties of the localized activity are described in section 4. A discussion follows in section 5.

## 2. Experiments

### 2.1. Diagnostics

In ASDEX Upgrade (AUG), magnetic pick-up coils are installed for measuring the time derivative of the radial or poloidal magnetic field (figure 1). In particular, the ‘C09’ series of coils used in this study encircle a plasma poloidal cross-section at a fixed toroidal position, and measures  $\dot{B}_\theta$  with a 2 MHz sampling rate. In addition, the ‘ballooning coil’ B31–03 (also with a 2 MHz sampling frequency) will be used in this analysis: it is located near the mid-plane and measures the time derivative of the radial component of the magnetic field  $\dot{B}_r$ . During the 2020 campaign, four additional  $\dot{B}_\theta$ -coils located at the same poloidal position as C09–26 ( $\pm 2.7^\circ$ ) close to the outer divertor, but at different toroidal positions have been connected, shown as golden circles in figure 1(b). The figure also shows the poloidal and toroidal position of current measurements by shunt resistors on the outer divertor tiles. The sampling frequency of the measurement is 200 kHz and the shunts are connected to the data acquisition system through an isolation amplifier with a 30 kHz low pass filter.

### 2.2. Plasma conditions

The analysis presented in this paper is mainly based on the AUG plasma discharge #34347 from the 2017 experimental campaign ( $I_p = 0.8$  MA, magnetic field  $-2.4$  T), presented in figure 2. It is an H-mode Deuterium plasma with moderate heating (2.6 MW of NBI, 1.2 MW of ECRH), low triangularity ( $\delta \simeq 0.26$ ), and a lower single null configuration. No external magnetic perturbations are applied. In the first phase of the discharge ( $2 < t < 5$  s), type-I ELMs occur at a repetition rate of  $\sim 50$  Hz, sometimes interrupted by smaller ‘ELM-like’ events. This phase is typical of H-mode plasmas used for inter-ELM mode studies at AUG, and the edge MHD modes occurring in similar discharges have been described elsewhere [11, 12]. When  $t > 5$  s, the density is increased by Deuterium fuelling, leading to more frequent and weaker crashes, while the large ELMs gradually disappear. These weaker events will hereafter be referred as ‘small ELMs’; their appearance is probably favoured by the increased density and the lower ratio between the injected power and the L-H power threshold. The average ELM repetition rate for  $t > 6.5$  s is 370 Hz.

In order to use the four additional  $\dot{B}_\theta$  coils located close to the outer divertor, which were connected in 2020 and not available for #34347, an additional discharge has been included in the analysis: the H-mode Deuterium plasma #37681 (from the 2020 campaign), with a plasma current of 1 MA, NBI and ECRH heating power of 2.5 and 2.8 MW respectively, a line-averaged density of  $8 \times 10^{19} \text{ m}^{-3}$ , and a low triangularity.

Note that the ELM and inter-ELM behaviours described in the following sections for these two discharges have also been observed in other plasmas (e.g. in about ten other H-mode discharges, in the context of developing and testing the analysis tools used for this work), and are therefore thought to be representative of a widespread behaviour in H-mode lower single null plasmas with type-I ELMs and no externally applied magnetic perturbations. However, existence diagrams in parameter space or sensitivity studies are beyond the scope of this work.

## 3. Poloidal localization of the explosive onset of ELMs

In this section, it is shown that the start of the explosive phase of both large and small ELMs, when observed from the poloidal array of magnetics, is poloidally localized in the X/OSP region.

To begin with, a typical behaviour for a single large ELM is presented in figure 3. The  $\dot{B}_\theta$  are shown at the start of a type-I ELM (panels (b) and (c)) and during an inter-ELM phase (panel (d)). These  $\dot{B}_\theta$  signals are normalized to their respective coil-dependent inter-ELM standard deviations, noted  $\sigma_{\text{inter}}$ . The series of  $\sigma_{\text{inter}}$  coefficients are calculated during the phase with large ELMs (2.5–5 s), for times to the nearest large ELM between  $-9$  and  $-4$  ms (noting  $t_{\text{ELM}}$  the ELM times, and  $\Delta t_{\text{ELM}} = t - t_{\text{ELM}}$  the time to the nearest ELM). Thus, for the signal  $s$  from a given coil,  $\sigma_{\text{inter}}^2[s] = \sum_{i=1}^N (s_i - \bar{s})^2 / N$ , where the sum is over the set  $\{s_i\}_{1 \leq i \leq N}$  of samples belonging to the specified temporal and ELM-synchronized windows, and  $\bar{s}$  is the mean value.

On the coils located near the outer strike point (C09–24, 25, 26 and 27), an activity is observed during most of the inter-ELM phase: it will hereafter be referred to as X/OSP activity or oscillation. Its inter-ELM properties will be further characterized in section 4. As shown in plots 3(b) and (c), at the beginning of an ELM, the amplitude of this oscillation grows before all other signals from the poloidal array.

It will now be shown more systematically that the poloidally localized start of the explosive phase of ELMs is a robust trend for the large and small ELMs of the analysed discharge. Our distinction between large and small ELMs relies on the routine ELM detection based on the induced peaks in the divertor currents: events with a peak below the detection threshold (i.e. with a geometric mean of the outer and inner divertor peak currents below 30% of the maximum value, for #34347 this corresponds to a threshold of 5.7 kA) will be referred to as small ELMs in the following. In the discharge #34347, 213 large ELMs and 661 small ELMs are analysed.

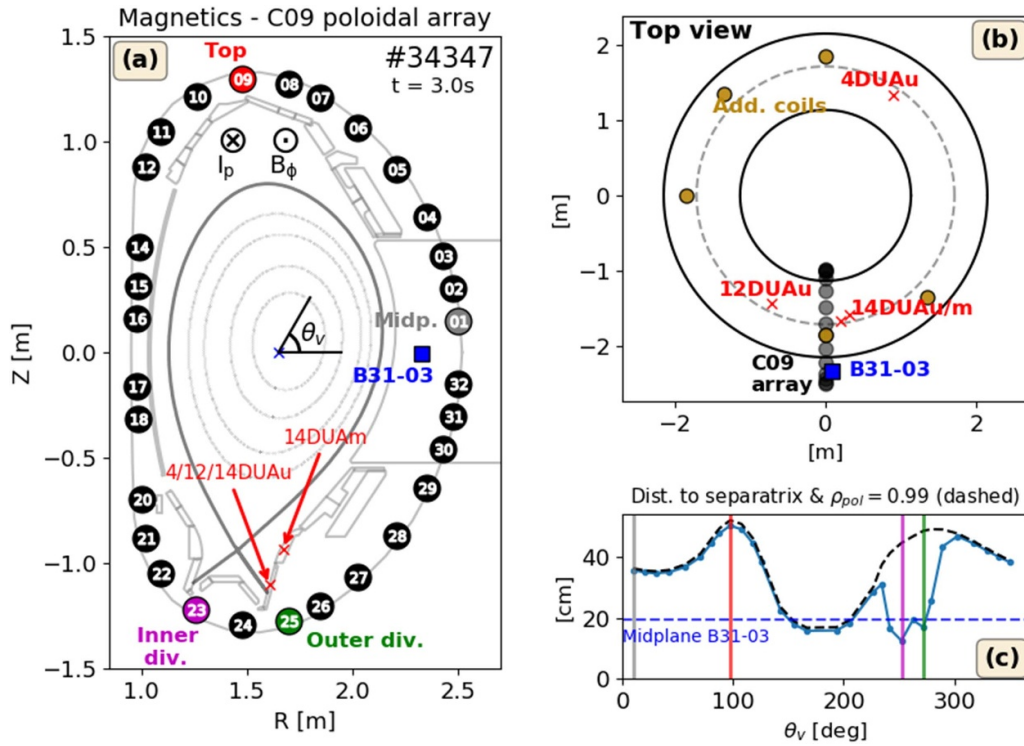


**Figure 1.** (a) Poloidal cross-section and (b) top view of ASDEX Upgrade, showing the plasma equilibrium, the location of the magnetics (coils from the C09 poloidal array are represented by the black circles, the ballooning coil B31-03 by the blue square, and the outer divertor  $B_\theta$  coils connected in 2020 by the golden circles), and the position of divertor tile current measurements (referred to as 4/12/14DUAu, and 14DUAm). (c) Minimum distance between the C09 coils and the separatrix including the inner/outer legs (plain dotted line), or the  $\rho_{pol} = 0.99$  surface (dashed line), as a function of the coil poloidal vacuum angle  $\theta_v$ , defined from the machine centre in panel (a). The vertical lines show the poloidal position of the C09-01/09/23/25 coils, respectively located near the outer mid-plane, the plasma top, the inner divertor and the outer divertor. These positions will be indicated with the same colour code throughout this paper.

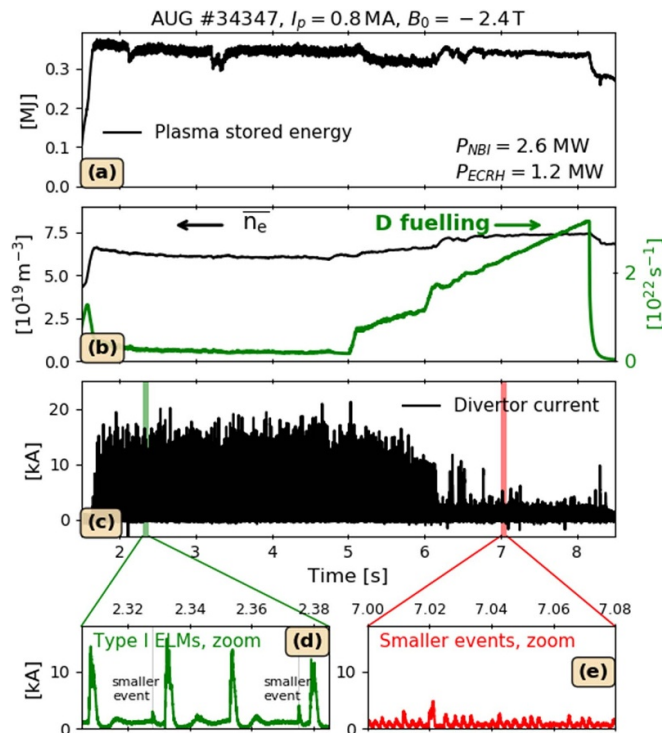


**Figure 2.** Time traces of (a) the plasma stored energy, (b) the line-averaged density  $\bar{n}_e$  measured by a central interferometry chord, and the Deuterium fuelling rate, (c) current on the inner divertor used as an ELM monitor (d) and (e): zooms in time windows of 80 ms showing the inner divertor current during phases with large and small ELMs.

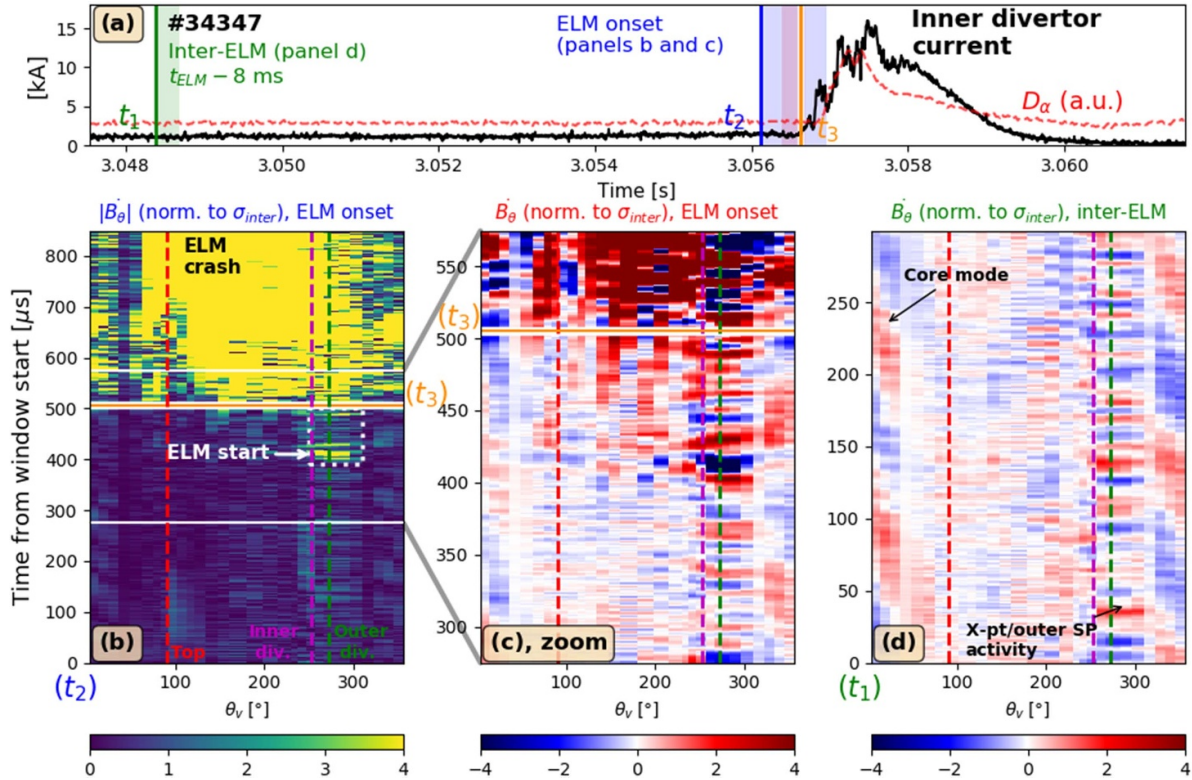


**Figure 3.** Start of an ELM during discharge #34347. (a) Current at the inner divertor (black, solid line) and  $D_\alpha$  radiation (red, dashed line). The vertical lines indicate several times of interest used in the following plots:  $t_1 = 3.0484$  s is the start of the inter-ELM window shown in panel (d);  $t_2 = 3.0561$  s is the start of the ELM window of panel (b);  $t_3 = 3.0566$  s is the time at which the inner divertor current starts to increase and is indicated by an orange horizontal line in panels (b) and (c). (b) Colourmap of the  $|B_\theta|$  signals from the C09 poloidal array (in absolute amplitude, and normalized to their respective inter-ELM standard deviations  $\sigma_{inter}$ , defined in the text), as a function of the poloidal position  $\theta_v$ , during the time window which starts at  $t = t_2$  showing the ELM start. The poloidal positions of the magnetic measurements at the plasma top (C09–09, red), at the inner (C09–23, magenta) and outer (C09–25, green) divertors are indicated by the dashed vertical lines. (c) Zoomed portion of panel (b), showing the (algebraic) normalized  $B_\theta$ . The magnetic activity near the outer divertor increases  $\sim 100 \mu$ s before  $t = t_3$  (start of inner divertor current rise). (d) For comparison, normalized  $B_\theta$  (same colour scale as in panel (c)) during the inter-ELM window starting at  $t_1 = 3.0484$  s. The magnetic activity in the outer divertor region is also visible, but at a lower level than at the ELM start.

The procedure described below is applied to study the ELMs starting phase using the C09 poloidal array of magnetics. We first define a series of coil-dependent thresholds above which the  $B_\theta$  signals are considered to have reached an ELM level: thresholds of 4 times the inter-ELM standard deviation  $\sigma_{inter}$  have been chosen. In the inter-ELM window used for the  $\sigma_{inter}$  determination, at least 99% of the samples of each coil are below the corresponding  $4\sigma_{inter}$  level. Then, for each ELM event, and for each coil, the first crossing of the  $4\sigma_{inter}$  threshold is picked. Thus, the poloidal ‘starting location’ of every single ELM is defined as the angle of the coil where the  $B_\theta$  first rises above its threshold. Expressed mathematically, if we note  $t_{start}^j[i]$  the threshold-crossing time at the coil  $i$  for a given ELM  $j$ , then the ELM starting time will be defined as the minimum value when considering all C09 coils<sup>3</sup>  $t_{start}^j \equiv \min_i t_{start}^j[i]$ ; and the time lag at coil  $i$  with respect to  $t_{start}^j$  is noted  $\Delta t_{start}^j[i] \equiv t_{start}^j[i] - t_{start}^j$ .

<sup>3</sup> Thus, the time  $t_{start}$  is a precise determination of the ELM starting time from magnetics. It differs from  $t_{ELM}$  which is calculated from the divertor currents with less precision, and sometimes used in the following sections (e.g. inter-ELM studies) when no precise timing is required.

The distributions of starting locations and time lags  $\Delta t_{start}$  are shown in figure 4 for the large and small ELMs. The trends are very similar for the two types of events, with a distribution of starting poloidal locations peaked near the outer divertor. This confirms the trend presented in figure 3. From this main starting location, the ELMs develop—on average—poloidally both towards the low field and the high field side, as visible in the  $\Delta t_{start}$  distributions. This common property of large and small ELMs suggests some similarity in the mechanism causing their explosive phase. One small difference is that the average poloidal development is slightly faster for large ELMs ( $\sim 100 \mu$ s) than for small ELMs ( $\sim 150 \mu$ s).

Note that it has been checked that the above analysis is not biased by an increase of the ELM  $4\sigma_{inter}$ - thresholds induced by the core modes. Indeed, when the analysis is re-done after first performing a high-pass filtering to remove the core modes, the resulting distributions of ELMs starting locations are similar to those shown in figures 4(a) and (c).

It is interesting to note that during Limit Cycle Oscillations close to the power threshold of L-H transitions, the magnetic activity was also found to propagate from the same poloidal location [13]. A poloidal localization of the radiation near the

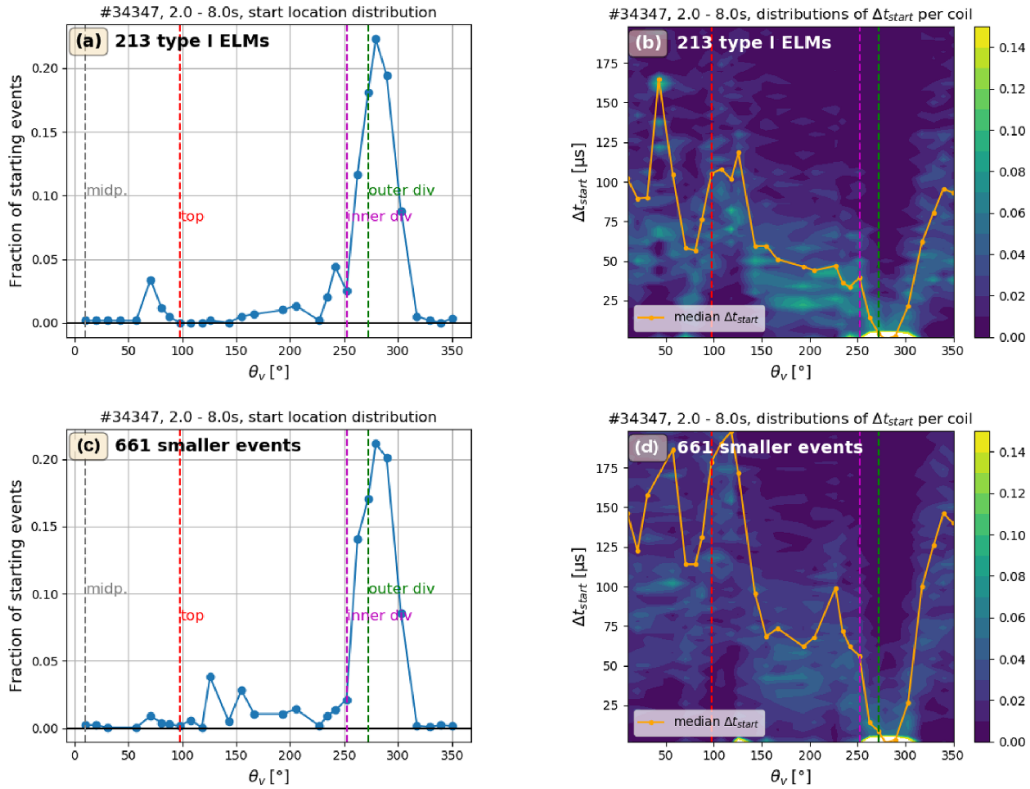


**Figure 4.** (a) Poloidal distribution of starting locations of large ELMs, as a function of the poloidal angle of the coils  $\theta_v$ . The fraction of starting events (plotted on the y-axis) is defined as the ratio between the number of events (here, large ELMs) starting at one coil to the total number of events. (b) Series of distributions of the time lags  $\Delta t_{\text{start}}$  for each coil of the poloidal array.  $\Delta t_{\text{start}}$ , defined in the text, is the time lag between the ELM start at a given coil and the minimum ELM start time on the whole C09 poloidal array. The median values of  $\Delta t_{\text{start}}$  are indicated by the overlaid curve. (c) and (d) Similar plots than in panels (a) and (b) for small ELMs.

X point at the start of ELMs has been also reported on TCV [14].

To check that this observed start of the explosive phase is not an artifact related to the variable distance between the magnetic coils and the plasma edge (see figure 1(c)), a comparison with the  $\dot{B}_r$  signal measured by the ‘ballooning coil’ B31–03 is shown on figure 5. B31–03 is toroidally located close to the poloidal C09 array (toroidal separation of only  $1.8^\circ$ ), but 16 cm closer to the separatrix than the corresponding coil C09–01. The logarithmic plot of the root mean square (RMS) value calculated over a  $20 \mu\text{s}$  moving window shows that the strong rise of the C09–25 signal (close to the outer strike point) occurs  $\sim 80 \mu\text{s}$  before the mid-plane signal in this typical example. Such a temporal shift is consistent with the expected delay  $\Delta t_{\text{start}}$  at the outer mid-plane, see figure 4(b). This shows that the delay of C09–01 with respect to C09–25 is not due to its larger distance to the separatrix.

In addition, there are no indications of an enhanced sensitivity of C09–25 to modes from the confined region, which might have explained the observation of figure 5 if the growing perturbation was initially below the detection level at the midplane magnetics. Indeed, there is no signature in the C09–25 inter-ELM spectra of the low frequency core mode (visible in figure 3) and of the edge pedestal mode detected by the edge ECE channels [15].

Figure 5 also plots an estimate of the growth rates of  $\dot{B}_r$  and  $\dot{B}_\theta$  at the start of the explosive phase, which are in the range  $2 - 5 \times 10^4 \text{ s}^{-1}$ . Thus, the ELM development is  $\sim 2 - 3$  times faster than predicted in recent non-linear simulations [16].

#### 4. Inter-ELM properties of the X/outer strike point activity

We have shown that the magnetic activity poloidally localized in the region of the outer strike point is also present during the inter-ELM phase. To gain a better understanding of the nature of this phenomenon, its inter-ELM properties are described in this section.

##### 4.1. Spectral properties

By comparing the  $\dot{B}_\theta$  signals recorded at different poloidal locations, it appears that the X/OSP activity has some specific spectral properties. In figure 6, the inter-ELM spectra from the coils of the poloidal array are displayed. These spectra are taken from the phase dominated by large ELMs (#34347,  $2 - 5 \text{ s}$ ), and conditionally averaged relatively to the time to the nearest large ELM ( $-10 \leq \Delta t_{\text{ELM}} \leq -2 \text{ ms}$ ). All signals are normalized to the inter-ELM standard deviation  $\sigma_{\text{inter}}$  before

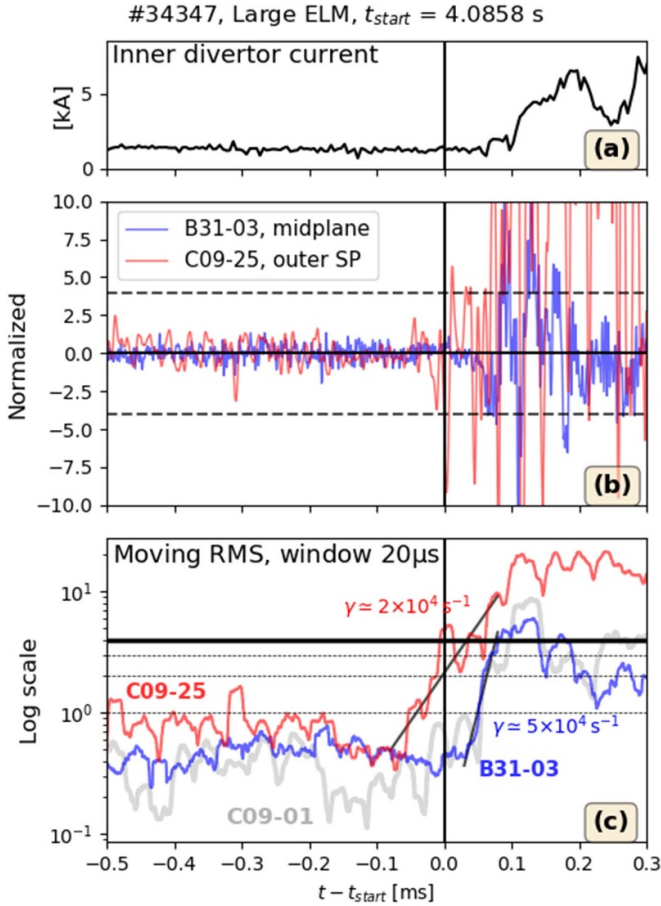


**Figure 5.** Comparison between  $\dot{B}_\theta$  measured at the outer divertor by the C09–25 coil, and  $\dot{B}_r$  measured by B31–03 close to the mid-plane, and toroidally separated from the C09 array by  $1.8^\circ$ . (a) Inner divertor current, used as an ELM monitor. (b) B31–03 and C09–25 signals, at the ELM start, normalized to their inter-ELM standard deviation  $\sigma_{\text{inter}}$ . The horizontal dashed lines indicate the ELM  $4\sigma_{\text{inter}}$  threshold. (c) Logarithmic plot of the corresponding RMS calculated in a moving  $20\ \mu\text{s}$ -long window, showing the delayed rise at the mid-plane and estimates of the growth rates. The plot also includes the moving RMS of C09–01 (outer midplane  $\dot{B}_\theta$ ). The growth rates  $\gamma$  of B31–03 and C09–25, which are obtained from the linear fits shown in the plot, are annotated.

the spectra are calculated. The region of the X/OSP activity corresponds to a broadband spectra extending up to approximately 100 kHz. This feature is absent at other poloidal angles, where narrow peaks are detected, in the low-frequency region ( $<10\ \text{kHz}$ , corresponding to core modes), around 75 kHz, and 220 kHz. Note that in the case of upper single null plasmas, the broadband spectra are observed on the magnetics located at the plasma top, showing it is causally related to the presence of an X-point.

The ELM-synchronized spectra are shown in figure 7 for three magnetic coils: the outer divertor coil C09–25, and two coils located near the mid-plane: C09–01 ( $\dot{B}_\theta$ ) and B31–03 ( $\dot{B}_r$ ). The C09–25 spectra retain their broadband shape during the ELM crash. This contrasts with the spectra from the mid-plane coils, whose shape changes during ELMs. The similar

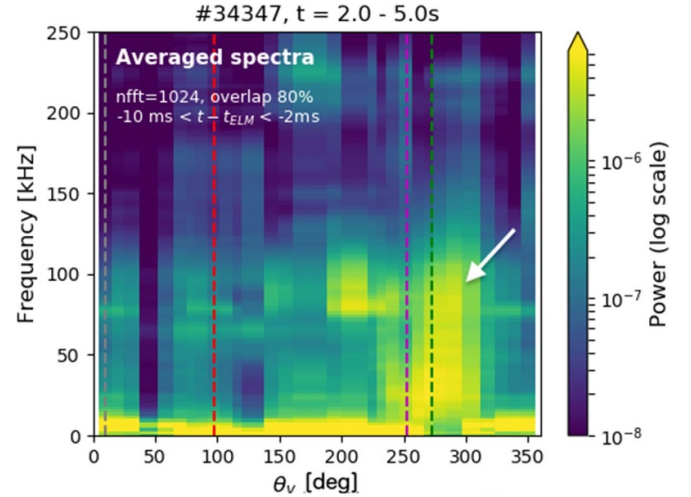


**Figure 6.** Conditionally averaged spectra of the magnetics signal from the poloidal array, during the phase with type-I ELMs #34347,  $2 < t < 5\ \text{s}$ , for  $-10 < \Delta t_{\text{ELM}} < -2\ \text{ms}$ . The arrow indicates the region of broadband inter-ELM activity poloidally located close to the outer divertor.

spectral shape kept by the C09–25 spectra suggests that it is a similar kind of activity that may dominate the  $\dot{B}_\theta$  signal at this location during both ELMs and inter-ELM phases. This is also consistent with the temporal behaviour at an ELM start shown on figure 3(c).

An examination of the C09–25 (outer strike point) signal reveals that these  $\dot{B}_\theta$  fluctuations are not really ‘broadband’, in the sense of a sum of widely distributed modes with stationary spectral properties. Indeed, as can be seen in the spectrogram shown in figure 8 done using a shorter  $128\ \mu\text{s}$ -long time window, the signal rather consists of a disorganised succession of short-lived ( $\sim 100\ \mu\text{s}$ ) fluctuations, distributed in a large frequency range ( $\sim 15 - 80\ \text{kHz}$  in this example). This results in an apparent broadband spectrum when longer time windows are used for the fast Fourier transform (FFT) calculations, as done in figure 6.

#### 4.2. Poloidal correlation analysis and propagation

The apparent poloidal propagation of the X/OSP activity is studied using correlation analysis. The cross-correlation function of two real time series with zero mean,  $x(t)$  and  $y(t)$ , can be defined as  $\rho_{xy}(\tau) = \int x(t)y(t+\tau)dt / \sigma_x\sigma_y$ , where  $\sigma_x^2 = \int |x(t)|^2 dt$ ; it satisfies  $-1 \leq \rho_{xy} \leq 1$ . The cross-correlation time delay  $\tau$  is when the maximum value of the cross-correlation  $\rho_{xy}(\tau)$  is reached. Each  $\dot{B}_\theta$  signal from the poloidal array is cross-correlated with a reference coil, here chosen to be C09–26, located near the outer divertor. Note that C09–26 has been selected rather than C09–25 because of a small temporal advance of C09–26, as shown in the following—in any case, the measurements from these two coils are highly correlated. To attenuate low-frequency core modes, all signals have been high-pass filtered (cut-off frequency 12 kHz) before calculating a series of cross-correlations in  $100\ \mu\text{s}$ -long

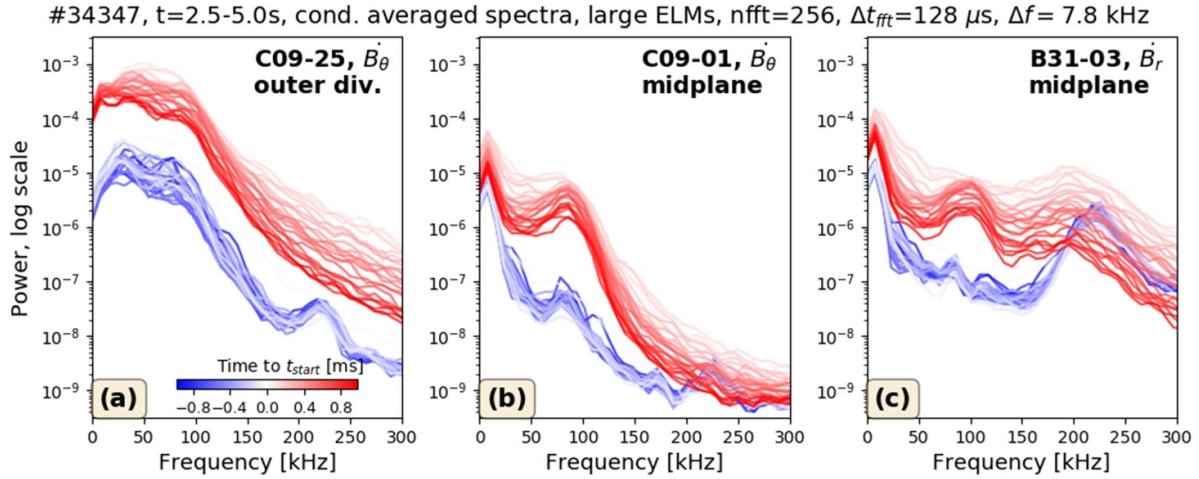


**Figure 7.** Conditionally averaged spectra during the phase dominated by type-I ELMs ( $2.0 < t < 5.0$  s), for three magnetic coils: (a) C09–25 (outer divertor,  $B_\theta$ ); (b) C09–01 (mid-plane,  $B_\theta$ ); (c) B31–03 (mid-plane,  $B_r$ ). Unlike B31–03 and C09–01, the average shape of the C09–25 spectra remains qualitatively similar during an ELM.

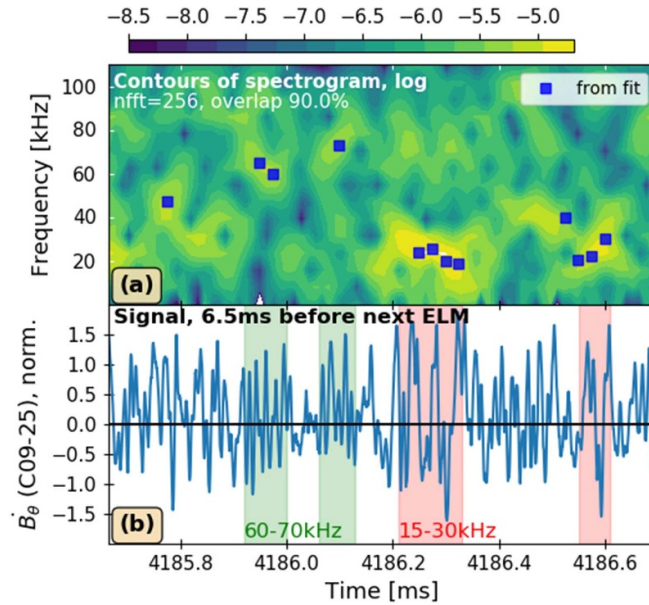


**Figure 8.** (a) Spectrogram of the signal from coil C09–25 (outer divertor), calculated using a short time window of 256 points ( $\Delta t = 128 \mu\text{s}$ ), with a 90% overlap. Dominant frequencies evaluated using a sinusoidal fit in short time-windows are represented by the blue squares. (b) Corresponding signal, showing short-lived oscillations dominated by different frequencies in the range 15–80 kHz.

windows, which are then conditionally averaged according to the time to the nearest ELM. The results are shown in figure 9. The region of large correlation is narrow in the poloidal direction  $\Delta\theta_v \sim 60^\circ$ , and located in the vicinity of the outer divertor. Figure 9(c) shows the evolution of the time-delay profiles. They present an apparent ‘V-shaped’ propagation in two opposite poloidal directions from the reference coil signal. This contrasts with the signature expected from a rotating mode located inside the separatrix, which should be a monotonic time-delay poloidal profile. The small time delays ( $\lesssim 1.5 \mu\text{s}$  for a poloidal separation of  $\sim 50^\circ$ , see figure 9(c)) indicate a very rapid apparent poloidal propagation approaching  $600 \text{ krad s}^{-1}$ , i.e. much higher than the typical rotation

rates at the pedestal  $E \times B$  velocity. However, it is not excluded that the small time lags could be due to geometrical effects: for example, in presence of a large tilted structure which would be detected almost simultaneously by the different coils.

#### 4.3. Outer divertor tile currents

It is demonstrated in this paragraph that the X/OSP activity is also detectable on the divertor current measurement of the outer strike point tile.

In figure 10, cross-spectrograms between the divertor tile currents and the  $B_\theta$  signal from C09–25 (outer divertor) are shown during an inter-ELM phase. A significant cross-power

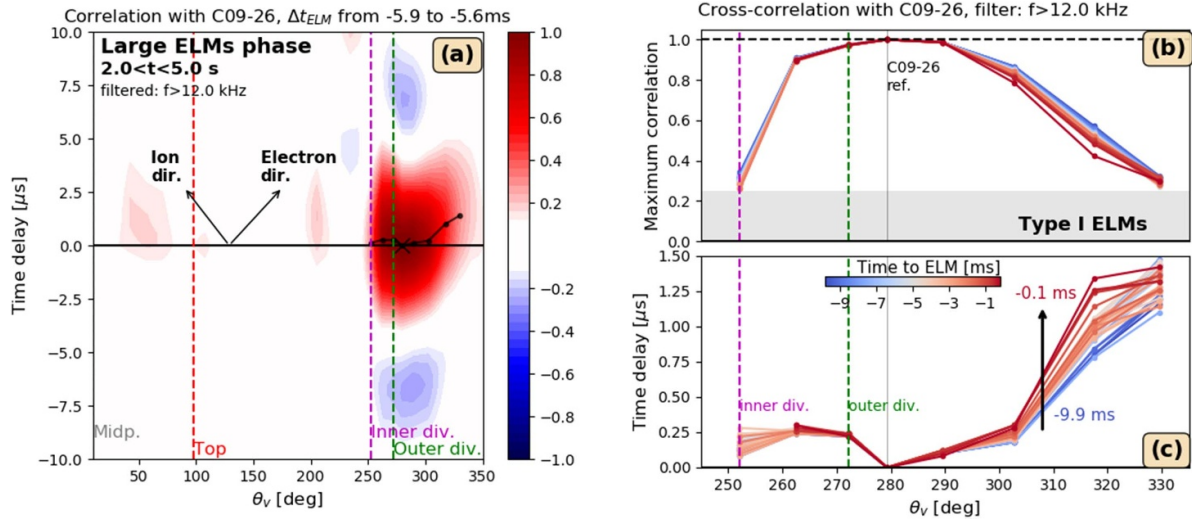


**Figure 9.** (a) Colourmap plot of the series of cross-correlation functions with the reference coil C09–26 (outer divertor), as a function of the poloidal angle of the cross-correlated coil and the time delay. The correlations are conditionally averaged according to time to the nearest large ELM,  $\Delta t_{\text{ELM}}$ . In this plot, averaged cross-correlations in the interval  $-5.9 \text{ ms} \leq \Delta t_{\text{ELM}} \leq -5.6 \text{ ms}$  are represented. The solid dotted line indicates the time delays of maximum correlation. Two arrows show the directions of the poloidal projections of the ion diamagnetic drift (noted ‘Ion dir.’) and electron diamagnetic drift (‘Electron dir.’). (b) Maximum values of the cross-correlations as a function of the poloidal angle of the coil cross-correlated with the reference. The various lines are for different values of the time to ELM  $\Delta t_{\text{ELM}}$ , see colour code in panel (c). (c) Series of cross-correlation time delays corresponding to the maximum values plotted in panel (b) (maxima associated with a cross-correlation below 0.25 are not represented), with a colour code to indicate the time to the nearest ELM (an evolution towards larger time delays when approaching the next ELM can be noted, though the underlying reason is unclear).

is observed between C09–25 and the divertor current from the outer strike point tile (panels (a) and (b)): after an episode of high-frequency fluctuations  $\sim 40\text{--}60 \text{ kHz}$  approximately 8 ms after the first displayed ELM, the cross-spectra are dominated by frequencies in the  $10\text{--}40 \text{ kHz}$  range. In contrast, almost no cross-power is detected between C09–25 and the divertor current from the tile 14DUAm (panel (c)). The tile of the outer strike point (14DUAu or ‘near SOL’) collects the SOL field lines with  $\rho_{\text{pol}} < 1.035$  and a part of the private flux region; the tile above (14DUAM or ‘far SOL’) collects field lines in the far SOL with  $1.035 < \rho_{\text{pol}} < 1.075$ .

In figure 11, the previous trend is confirmed on a more systematic basis by calculating a series of coherences between the divertor currents from the near/far SOL tiles and all the  $\hat{B}_\theta$  measurements from the poloidal array. The coherence between two signals  $x$  and  $y$  lies between 0 (uncorrelated) and 1 ( $x$  and  $y$  linearly dependent), and is defined as  $|S_{xy}|^2 / S_{xx}S_{yy}$ , where  $S_{xy}$  and  $S_{xx}$  are the cross-spectral and auto-spectral density functions. Here, these quantities are evaluated by conditional averaging on 2048 points-long FFT windows in the interval  $-10 \leq \Delta t_{\text{ELM}} \leq -2 \text{ ms}$ , taken during the phase with large ELMs,  $3.0 \leq t \leq 4.5 \text{ s}$ . Using the divertor current from the near SOL tile as a reference (figure 11(a)), significantly large coherences with the magnetics near the outer divertor are observed in the frequency range  $\sim 15\text{--}40 \text{ kHz}$ ; with peak values around  $\sim 0.3$ . The coherences between the reference divertor current and magnetics at the outer mid-plane are much lower: less than 0.004 with C09–01 in the frequency interval  $15\text{--}40 \text{ kHz}$  (similar low values are obtained with the mid-plane ballooning coil B31–03, located closer to the plasma, showing that the loss of

coherence at the mid-plane is not due to the distance between the magnetics and the SOL). This region of large coherence is not observed when the reference divertor current is taken from the far SOL tile (figure 11(b)); this sets an upper radial limit of  $\rho_{\text{pol}} = 1.035$  for the possible localization of the electric currents associated with the X/OSP activity.

The poloidal localization of the region of large coherence at  $15\text{--}40 \text{ kHz}$  in figure 11(a) allows to exclude the possibility of a motion of the whole plasma column as an explanation. The expected signature of such a global equilibrium perturbation on the coherence maps of figures 11(a) and (b) would have been a region of large coherence at all poloidal angles.

Therefore, we conclude that the observed X/OSP magnetic activity is associated with currents connected to the outer divertor target: either in the private flux region or in the near-SOL  $\rho_{\text{pol}} < 1.035$ .

#### 4.4. Toroidal mode numbers and propagation

The toroidal structure of the X/OSP activity is studied in the H-mode phase of discharge #37681 (lower single null, plasma current of 1 MA, NBI and ECRH heating power of 2.5 and 2.8 MW respectively, line-averaged density of  $8 \times 10^{19} \text{ m}^{-3}$ ) using the four additional  $\hat{B}_\theta$  coils shown in figure 1(b). They have the same poloidal location as C09-26 near the outer strike point (within  $2.7^\circ$ ). Thus, a series of 5 coils with a minimum toroidal angular separation of  $45^\circ$  is available, allowing to resolve toroidal mode numbers  $|n| \leq 4$ . The toroidal mode numbers are evaluated from a linear fit of

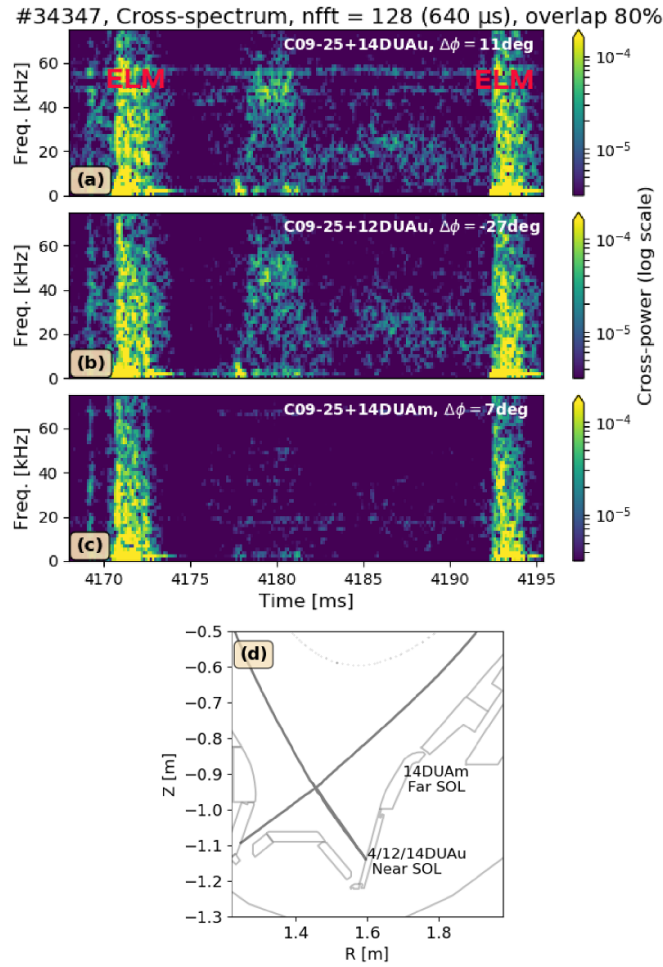


**Figure 10.** Cross-spectral amplitude of C09–25 signal ( $\vec{B}_\theta$ , outer divertor, downsampled to 200 kHz) with the divertor currents measured on three tiles at the outer divertor: (a) and (b) ‘near SOL’ outer target tiles 14DUAu and 12DUAu, (c) ‘far-SOL’ tile 14DUAm without strike point. The toroidal separations  $\Delta\phi$  between the cross-correlated signals are indicated. (d) Tiles location.

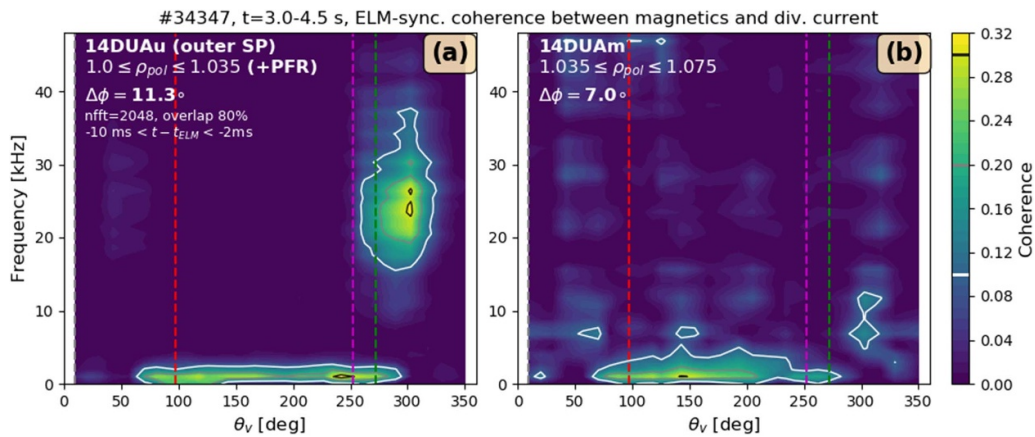


**Figure 11.** Coherence between the magnetics from the C09 poloidal array and two divertor currents measurements: (a) from the ‘near SOL’ tile 14DUAu (outer target,  $\rho_{pol} < 1.035$  plus part of the private flux region); (b) divertor currents from the ‘far SOL’ tile 14DUAm ( $1.035 < \rho_{pol} < 1.075$ ). The cross-spectral and auto-spectral density functions in the coherence calculation are evaluated using conditional averaging for  $-10 \leq \Delta t_{ELM} \leq -2$  ms, in the time interval 3.0 – 4.5 s of discharge #34347.

the cross-phase as a function of the toroidal angular separation. The cross-phases are calculated using  $\sim 1$  ms-long FFT windows.

An example of inter-ELM spectrogram with corresponding toroidal mode numbers  $n$  is shown in figures 12(a) and (b). In the range 10–40 kHz,  $n = -1$  dominates (the minus

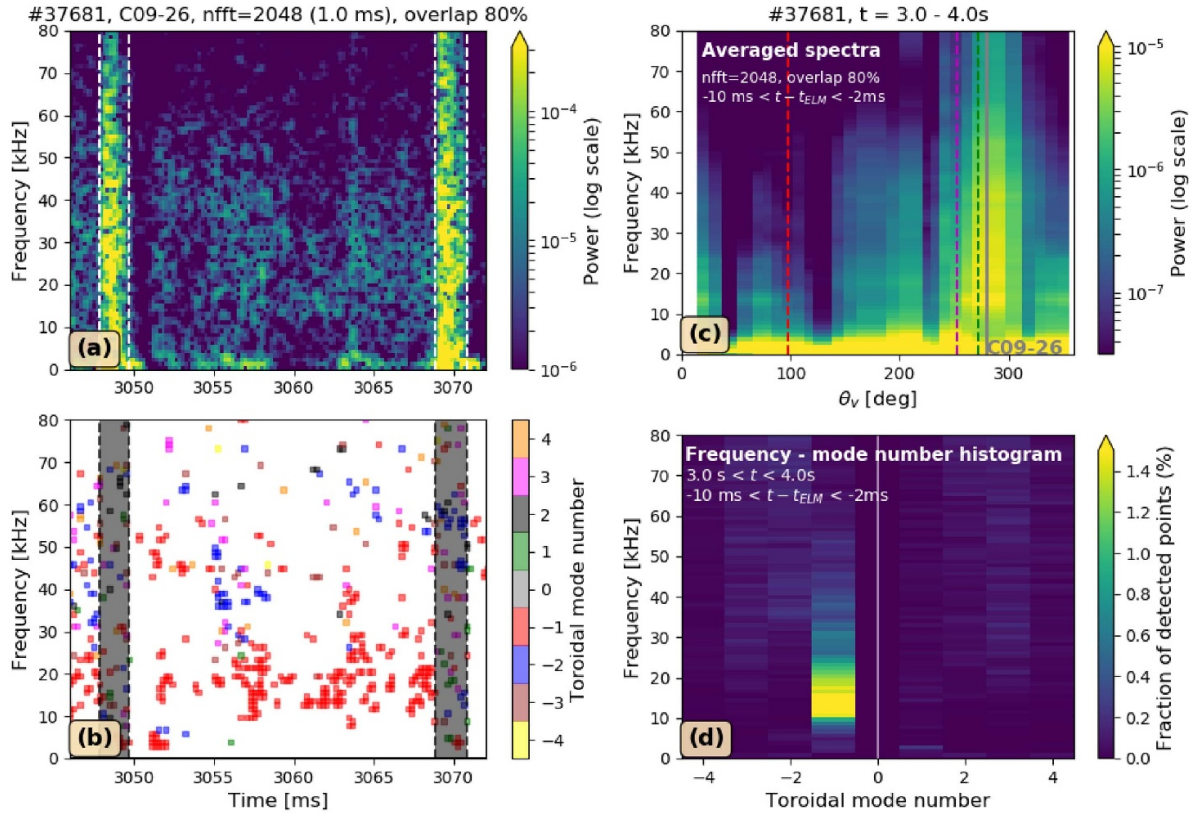


**Figure 12.** Mode number analysis for the X/OSP activity done in the auxiliary discharge #37681. (a) Spectrogram during an inter-ELM phase. (b) Corresponding detected toroidal mode numbers (only displayed for time and frequencies corresponding to a spectral power above the 60% percentile in the analysed frequency range 0–120 kHz). (c) Inter-ELM conditionally averaged spectra for  $-10 \leq \Delta t_{ELM} \leq -2 \text{ ms}$ , similar to the corresponding inter-ELM spectra of #34 347 shown in figure 6. (d) Frequency-mode number histogram for  $-10 \leq \Delta t_{ELM} \leq -2 \text{ ms}$ , obtained in a 1 s-long stationary ELMy H-mode phase.

sign stands for counter-current propagation). This is confirmed by the frequency-mode number histogram shown in figure 12(d), which includes a 1 s-long time period and an ELM-synchronisation window  $-10 \leq \Delta t_{ELM} \leq -2 \text{ ms}$ .

The toroidal propagation can be evaluated by cross-correlation analysis of this series of 5 outer divertor  $B_\theta$  coils. There are 10 coil pairs in total, but due to some redundancy in toroidal spacing this results in only 5 distinct non-zero toroidal separations  $\Delta\phi$ , plus the autocorrelation at  $\Delta\phi = 0$ . The signals are beforehand band-pass filtered at the frequency range of the oscillation (15–60 kHz). A series of  $200 \mu\text{s}$ -long time windows are conditionally averaged in the inter-ELM phase. The resulting cross-correlations ( $\Delta\phi$ -binned, i.e. averaged within each bin of toroidal separation  $\Delta\phi$ ) are shown in figure 13. The  $n = -1$  structure is confirmed by the negative correlation observed for  $\Delta\phi = 180^\circ$ . From a fit of the time delays of maximum cross-correlation, the estimated toroidal angular velocity is about  $215 \text{ krad s}^{-1}$ : this corresponds to a toroidal velocity of  $395 \text{ km s}^{-1}$  in the counter-current direction when multiplied by the coils' major radius.

In the paragraph below, we discuss this toroidal velocity to show that it is not consistent with the  $E \times B$  rotation rate of

a core or pedestal mode—in agreement with the conclusion from section 4.3 that the X/OSP activity is due to currents in the open field line region. The rotation in the plasma core is in the co-current direction due to the NBI injection, so the only region with perpendicular (binormal) rotation in the electron direction is the pedestal. The edge ‘ $E_r$  well’ velocity is estimated from Charge eXchange Recombination Spectroscopy (see e.g. [17]) to be around  $-15 \text{ km s}^{-1}$  at the outer mid-plane, in the electron diamagnetic direction. The corresponding apparent toroidal angular velocity is  $\Omega_{E \times B} = |v_{E \times B} / R \sin \alpha|$ , where  $\sin \alpha$  is the sine of the pitch angle ( $11.8^\circ$  at the outer mid-plane) and  $R$  the local major radius. This leads to  $\Omega_{E \times B} \sim 30 \text{ krad s}^{-1}$ , much lower (by a factor of 7) than the value found in figure 13. Note that  $v_{E \times B}$  is locally proportional to  $|R \sin \alpha|$ : due to the cancellation of this factor, the resulting  $\Omega_{E \times B}$  is then in principle a flux function independent of the poloidal location.

Furthermore, the X/OSP activity is also routinely observed in L-mode. When the toroidal cross-correlation analysis shown in figure 13 is applied to L-mode plasmas (not shown), even larger apparent toroidal velocities, typically  $\sim 500 \text{ km s}^{-1}$ , are usually found in spite of the lower  $E \times B$

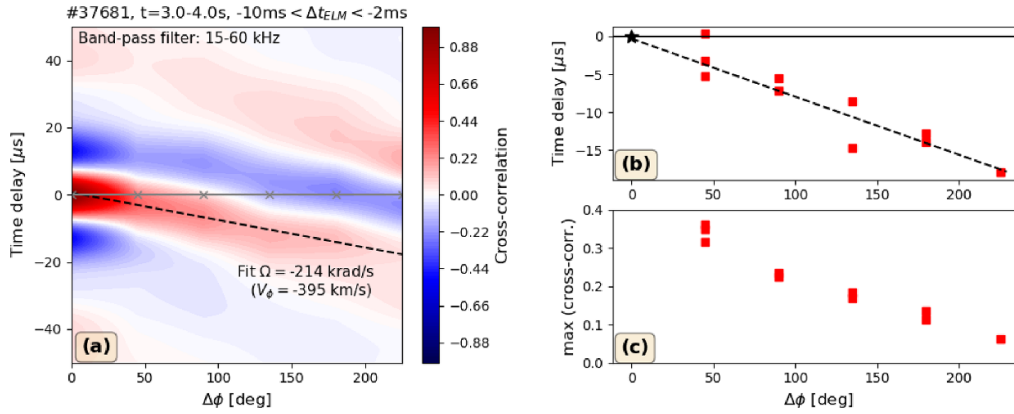


**Figure 13.** (a) Contour plots of the  $\Delta\phi$ -binned cross-correlations between the series of coils near the outer divertor, using the ELM-synchronisation window  $-10 < \Delta t_{\text{ELM}} < -2$  ms. The positions of the  $\Delta\phi$ -bins are indicated by the grey crosses on the y-axis. (b) Time delays at the cross-correlation maximum, for all pairs of coils located at the outer divertor. The dashed line corresponds to a robust linear fit and is also shown in panel (a). For  $\Delta\phi > 150^\circ$ , the correlation maxima with positive time delays are ignored. (c) Corresponding maxima of the cross-correlation.

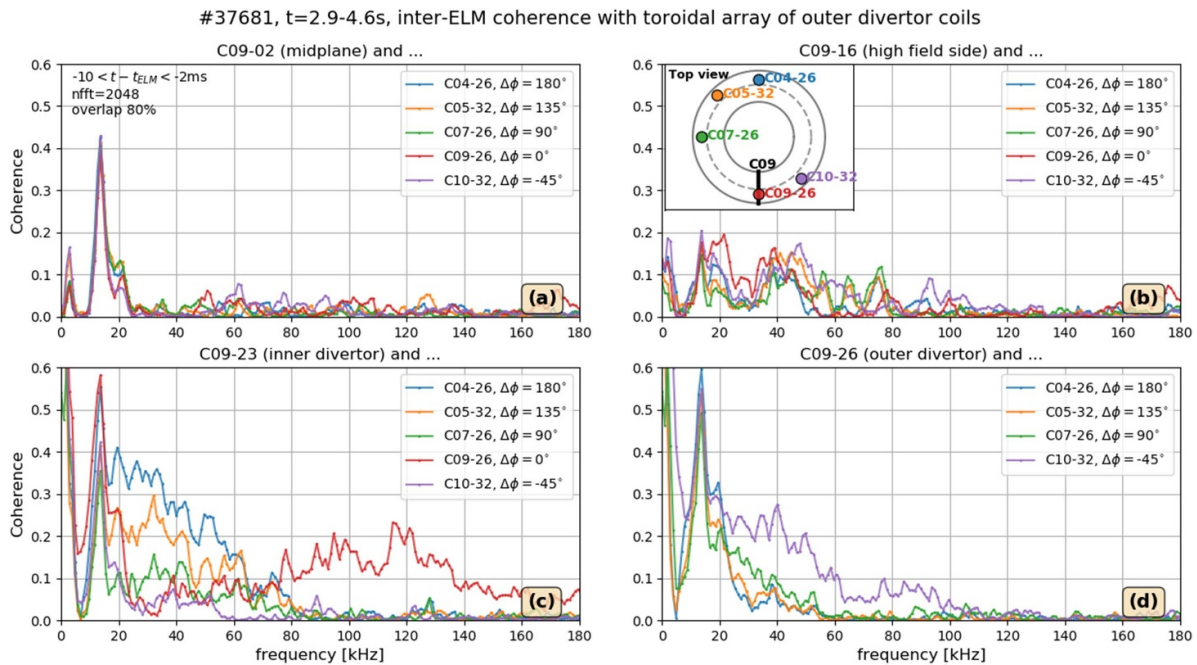


**Figure 14.** Inter-ELM coherences between the toroidal array of outer divertor coils, and the C09 magnetics from various poloidal positions. The analysis is done by coherent averaging of spectra of 2048 points taken in the temporal range  $-10 \leq \Delta t_{\text{ELM}} \leq -2$  ms. The toroidal position of the magnetics is indicated in the panel (b), and the toroidal separation is noted  $\Delta\phi$ . (a) Coherence with the outer midplane magnetic C09-02. (b) Coherence with the high field side magnetic C09-16, close to the inner midplane. (c) Coherence with the C09-23 magnetic close to the inner divertor, showing significant coherence between the inner and outer divertor coils toroidally separated by  $180^\circ$ . (d) Coherence with the C09-26 magnetic close to the outer divertor.

velocity in the pedestal. This is another indication that the observed propagation of the X/OSP activity is not related to a mode rotating at the pedestal velocity.

#### 4.5. Detection of the X/OSP perturbation at the inner divertor

More information on the 3D spatial structure of the perturbation can be inferred from the toroidal array of outer divertor magnetics, which detects the X/OSP activity at other toroidal locations. It is then possible to compare these signals to

those from the C09 poloidal array. By doing so, we can test if at a given poloidal position (e.g. outer midplane), the outer divertor activity from remote toroidal angles can be detected: this would be *a priori* conceivable if the corresponding closest SOL locations were connected by magnetic field lines.

The inter-ELM coherences between the series of outer divertor coils, and the C09 coils from four poloidal positions (outer midplane, high field side, inner divertor, outer divertor) are shown in figure 14. The analysis is performed on the H-mode plasma #37681 (2.9–4.6 s), described in section 2.2,

using coherent averaging on short time windows selected in the range  $-10 \leq \Delta t_{\text{ELM}} \leq -2$  ms.

The coherence between the outer divertor coils and the outer midplane coil C09–02<sup>4</sup> (panel (a)) is not significant apart from some low-frequency peaks (at about 3 kHz, 13 kHz, and possibly 20 kHz). No broadband coherence is found at the frequency range of the X/OSP activity 20–100 kHz, confirming the lack of detection of the X/OSP activity at the outer midplane.

The coherence with the high field side midplane coil C09–16 (panel (b)) is also low—although slightly higher than in the previous case. A faint detection is not excluded, but far from obvious, especially given that no clear dependence of the coherence with the toroidal separation is found.

However, comparisons with the inner divertor coil C09–23 (panel (c)) show an interesting behaviour. There is a broadband region ( $\sim 20$ – $80$  kHz) of significant coherence which reaches its maximum values when the toroidal separation is  $180^\circ$  (with C04–26). Broadband coherence between the inner and outer divertor magnetics at the same toroidal angle is also found in the range of  $\sim 70$ – $150$  kHz. Thus, the lowest frequency oscillations 20–80 kHz seem to be simultaneously detected by both the outer and inner divertor sections when they are  $180^\circ$  apart, while the higher frequency oscillations (70–150 kHz) are jointly detected at the inner and outer divertor sections with the same toroidal angle.

Finally, the coherences with the outer divertor coil C09–26 (panel (d)) show a broadband coherence decreasing with the toroidal separation, in agreement with the correlation analysis of figure 13. In the 20–60 kHz range, the coherence decays to ground levels when the toroidal separation increases from  $90^\circ$  (coherence between C07–26 and C09–26) to  $135^\circ$  (coherence between C09–26 and C05–32).

#### 4.6. Summary of inter-ELM observations

The inter-ELM properties of the X/OSP activity are:

- (i) Broadband spectra extending typically up to 100 kHz, due to the presence of many short-lived events of variable frequency.
- (ii) A poloidally localized region of observation in the outer-strike point region, with a cross-correlation decaying to low values for a poloidal separation of  $\sim \pm 30^\circ$ .
- (iii) A rapid ‘V-shaped’ apparent poloidal propagation towards both the low field and high field sides.
- (iv) Coherence between these oscillations and the currents in the divertor tiles of the outer strike point ( $\rho_{\text{pol}} < 1.035$ ).
- (v) An  $n = -1$  dominant toroidal mode number, and a toroidal propagation in the counter-current direction at a velocity close to  $400 \text{ km s}^{-1}$ , which is too large in comparison with the apparent velocity expected from a mode convected in the pedestal  $E \times B$  flow.

- (vi) Coherence between signals from outer and inner divertor magnetics separated by  $180^\circ$  (or by  $0^\circ$  at higher frequencies).

From these observations—especially the detection at the outer divertor tile, point (iv)—it is concluded that the X/OSP activity is due perturbed currents connected to the divertor targets. And as shown in section 3, the explosive phase of ELMs develops poloidally from the X/OSP region, following an initial growth of these perturbed currents. Thus, they appear as a key element in the causal chain of events triggering an ELM.

## 5. Discussion

Let us first discuss the nature of the X/OSP activity, before turning to its possible role in the triggering of ELMs.

The first question is whether the detected X/OSP activity is associated with perturbed structures which are parallel to the magnetic field. However, apart from the private flux region, magnetic field lines in the SOL encircle the poloidal plasma cross-section, which is difficult to reconcile with the lack of detection at other poloidal positions than the outer and inner divertors. Indeed, based on simple geometrical considerations, the perturbed poloidal magnetic field  $\delta B_\theta$  induced by a single current filament located at the closest separatrix position to a detector is roughly evaluated and found to remain within a moderate range of variations:  $0.4 \lesssim \delta B_\theta / \delta B_\theta[\text{C09} - 25] \lesssim 1.6$ , where  $\delta B_\theta[\text{C09} - 25]$  is the perturbed  $\delta B_\theta$  at the outer divertor coil C09–25. This is not sufficient to explain the absence of detection around the main plasma, unless some more complex—and less likely—effects such as a specific poloidal mode structure play a role.

The presence of the perturbation in the private flux region is not excluded, and is possibly consistent with the coherence found between the  $180^\circ$ -separated outer and inner divertor sections, see section 4.5. Yet, this is not fully satisfactory given the preferential detection of the X/OSP activity on the detectors from the outer divertor side (such as C09–25, 26, and 27, see figure 1).

Alternatively, the X/OSP activity could be due to a rotating 3D distortion of the separatrix itself. Indeed, non-axisymmetric perturbations in an X-point diverted plasma can cause the formation of lobes (or homoclinic tangles), whose associated displacements are much larger in the X-point region than at other poloidal locations [18]. One could expect that the rotation of a tangled separatrix causes a poloidally localized detection on the magnetics closest to the maximum radial displacements of the field lines, in general agreement with the analysis of section 4.

Next, let us mention some other experimental observations—done using diagnostics other than magnetics—of some disconnection or decorrelation between the outer divertor region and the main SOL above the X-point [19–25]. In particular, a category of filaments located below the X-point near the outer leg, and uncorrelated with the upstream mid-plane filaments has been identified on MAST, NSTX-U,

<sup>4</sup> C09–02 is used as the outer midplane coil instead of C09–01, whose measurements are not available for discharge #37 681.

and TCV [19, 20, 22, 25]. These ‘divertor filaments’ share some properties with the X/OSP activity: a short lifetime of the structures and similar frequencies of several tens of kHz. Further studies would be required to investigate if these filaments and the X/OSP activity are related. Note that effects such as the decorrelation of perturbations near the X-point [26], and the existence of modes localized in the divertor legs [27] have been predicted theoretically.

We now turn to the second part of the discussion on the causality between the X/OSP activity and the explosive onset of ELMs. While the mechanism causing the X/OSP activity is not fully identified, its probable role in the ELMs explosive onset has been shown in section 3. This is consistent with a previous observation from Takahashi *et al* that the earliest sign of an ELM is an increase in the SOL current measured at the divertor tile [28]. Such behaviour is not really expected from the linear peeling-ballooning theory. This does not indicate a contradiction; rather that some triggering mechanism could be localized in the X/OSP region, and play a role in a phase subsequent to the initial growth of a peeling-ballooning mode—which can remain in a saturated state during long periods of time [3].

Of possible relevance is the self-amplifying loop between non-axisymmetric currents and homoclinic tangles first proposed by Evans and co-workers to describe the non-linear evolution of ELMs [29–32]: field-aligned helical currents connecting the inner and outer divertors can reinforce pre-existing homoclinic tangles, creating more flux tubes connecting the targets through the confined region, and therefore allowing more helical current to flow, etc. The catastrophic cycle can be initiated by thermoelectric currents caused by an initial heat pulse arriving at the divertor from the pedestal region [29]—possibly as a consequence of pedestal MHD activity (e.g. peeling–ballooning modes). Thus, homoclinic tangles would not only be the ‘footprint’ of other non-axisymmetric perturbations present in the plasma but also be able to drive currents which play a role in the triggering of ELMs. This is consistent with the start of ELMs explosive phase localized in the X/OSP point region, and the  $\sim 100 \mu\text{s}$  delay of the explosive growth at other poloidal locations, as described in section 3.

## 6. Summary

The start of ELMs has been studied using an array of magnetics encircling a poloidal cross-section, in two AUG lower single null H-mode plasmas. It was shown that the onset of the explosive (associated with growth times of  $\sim 20\text{--}50 \mu\text{s}$ ) phase of type-I ELMs is poloidally localized in the X/OSP region. This indicates the presence of a triggering phenomenon in that region. From this location, ELMs develop on average towards the low-field and high-field sides in typically  $100 \mu\text{s}$ . A similar conclusion also holds for the small ELMs present in the first analysed discharge (#34347).

An associated magnetic activity localized in the X/OSP region is also observed at a lower level in-between ELMs. It is detected both by the magnetics located close to the outer

divertor and by the shunt resistors measuring divertor currents at the outer target ( $\rho_{\text{pol}} < 1.035$ ). The activity is therefore interpreted as being due to perturbed currents connected to the divertor targets. Its broadband spectra typically extend up to 100kHz—due to the presence of short-lived events of variable frequencies—and are dominated by  $n = -1$  toroidal mode numbers rotating in the counter-current direction.

## Acknowledgment

We would like to thank G. Birkenmeier, A. Cathey, M.G. Dunne, M. Hoelzl, F. Orain, C.P. Perez von Thun, A. Wingen, E. Wolfrum, Q. Yu and H. Zohm for helpful discussions; and S. Vorbrugg for providing CAD information. This work has been carried out within the framework of the EUROfusion Consortium, funded by the European Union via the Euratom Research and Training Programme (Grant Agreement No 101052200—EUROfusion). Views and opinions expressed are however those of the author(s) only and do not necessarily reflect those of the European Union or the European Commission. Neither the European Union nor the European Commission can be held responsible for them.

## ORCID iDs

E. Trier  <https://orcid.org/0000-0002-6901-8669>

P. Hennequin  <https://orcid.org/0000-0002-4848-4898>

L. Giannone  <https://orcid.org/0000-0001-5611-200X>

B. Vanovac  <https://orcid.org/0000-0003-4031-9318>

## References

- [1] Gunn J.P. *et al* 2017 *Nucl. Fusion* **57** 046025
- [2] Connor J.W., Hastie R.J., Wilson H.R. and Miller R.L. 1998 *Phys. Plasmas* **5** 2687
- [3] Perez von Thun C. *et al* 2019 *Nucl. Fusion* **59** 056004
- [4] Laggner F.M., Diallo A., Cavedon M. and Kolemen E. 2019 *Nucl. Mater. Energy* **19** 479
- [5] Perez C.P. *et al* 2004 *Plasma Phys. Control. Fusion* **46** 61
- [6] Yun G.S., Lee W., Choi M.J., Lee J., Park H.K., Tobias B., Domier C.W., Luhmann N.C., Donné A.J.H. and Lee J.H. 2011 *Phys. Rev. Lett.* **107** 045004
- [7] Boom J.E. *et al* 2011 *Nucl. Fusion* **51** 103039
- [8] Manz P., Boom J.E., Wolfrum E., Birkenmeier G., Classen I.G.J., Luhmann N.C. and Stroth U. (the ASDEX Upgrade Team) 2014 *Plasma Phys. Control. Fusion* **56** 035010
- [9] Kirk A., Dunai D., Dunne M., Huijsmans G., Pamela S., Becoulet M., Harrison J.R., Hillesheim J., Roach C. and Saarelma S. 2014 *Nucl. Fusion* **54** 114012
- [10] Diallo A., Dominski J., Barada K., Knolker M., Kramer G.J. and Mckee G. 2018 *Phys. Rev. Lett.* **121** 235001
- [11] Vanovac B. *et al* 2018 *Plasma Phys. Control. Fusion* **60** 045002
- [12] Mink F. *et al* 2018 *Nucl. Fusion* **58** 026011
- [13] Birkenmeier G. *et al* 2016 *Nucl. Fusion* **56** 086009
- [14] Veres G., Pitts R.A., Bencze A., Márki J., Tál B. and Tye R. (the TCV team) 2009 *J. Nucl. Mater.* **390–391** 835
- [15] Vanovac B. *et al* 2018 *Nucl. Fusion* **58** 112011

- [16] Cathey A. Hoelzl M., Lackner K., Huijsmans G.T.A., Dunne M.G., Wolfrum E., Pamela S.J.P., Orain F. and Günter S. 2020 *Nucl. Fusion* **60** 124007
- [17] Viezzer E. *et al* 2013 *Nucl. Fusion* **53** 053005
- [18] Evans T.E., Roeder R.K., Carter J.A. and Rapoport B.I. 2004 *Contrib. Plasma Phys.* **44** 235
- [19] Harrison J.R., Fishpool G.M. and Dudson B.D. 2015 *J. Nucl. Mater.* **463** 757
- [20] Walkden N.R., Harrison J., Silburn S.A., Farley T., Henderson S.S., Kirk A., Militello F. and Thornton A. (the MAST team) 2017 *Nucl. Fusion* **57** 126028
- [21] Maqueda R.J. and Stotler D.P. 2010 *Nucl. Fusion* **50** 075002
- [22] Scotti F., Zweben S., Soukhanovskii V., Baver D. and Myra J. 2018 *Nucl. Fusion* **58** 126028
- [23] Scotti F., Zweben S., Myra J., Maqueda R. and Soukhanovskii V. 2020 *Nucl. Fusion* **60** 026004
- [24] Nem R.D., Manz P., Juul Rasmussen J., Vianello N., Walkden N., Naulin V., Sieglin B., Herrmann A. and Brida D. (the ASDEX Upgrade Team) 2021 *Plasma Phys. Control. Fusion* **63** 065005
- [25] Wüthrich C. *et al* 2022 *Nucl. Fusion* **62** 106022
- [26] Farina D., Pozzoli R. and Ryutov D.D. 1993 *Nucl. Fusion* **33** 1315
- [27] Ryutov D.D. and Cohen R.H. 2004 *Contrib. Plasma Phys.* **44** 168
- [28] Takahashi H., Fredrickson E.D., Schaffer M.J., Austin M.E., Brooks N.H., Evans T.E., Jackson G.L., Lao L.L. and Watkins J.G. 2005 *32nd EPS Conf. Plasma Phys. (Tarragona, 27 June–1 July 2005)* vol 29 p 4.018
- [29] Evans T.E., Yu J.H., Jakubowski M.W., Schmitz O., Watkins J.G. and Moyer R.A. 2009 *J. Nucl. Mater.* **390–391** 789
- [30] Wingen A., Evans T.E., Lasnier C.J. and Spatschek K.H. 2010 *Phys. Rev. Lett.* **104** 175001
- [31] Rack M., Wingen A., Liang Y., Spatschek K.H., Harting D.M. and Devaux S. (JET EFDA contributors) 2012 *Nucl. Fusion* **52** 074012
- [32] Knolker M., Evans T.E., Wingen A., Bortolon A., Laggner F.M., Moyer R.A., Nazikian R. and Zohm H. 2019 *Nucl. Fusion* **59** 126020